

We are IntechOpen, the world's leading publisher of Open Access books Built by scientists, for scientists

6,900

Open access books available

186,000

International authors and editors

200M

Downloads

Our authors are among the

154

Countries delivered to

TOP 1%

most cited scientists

12.2%

Contributors from top 500 universities



WEB OF SCIENCE™

Selection of our books indexed in the Book Citation Index
in Web of Science™ Core Collection (BKCI)

Interested in publishing with us?
Contact book.department@intechopen.com

Numbers displayed above are based on latest data collected.
For more information visit www.intechopen.com



Cathode Electronic Structure Impact on Lithium and Sodium Batteries Parameters

Janina Molenda

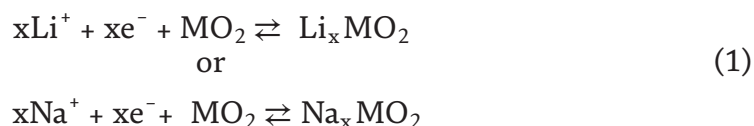
Abstract

The author of this work basing on her own investigations of A_xMO_2 cathode materials ($A = Li, Na$; $M = 3d$) has demonstrated that the electronic structure of these materials plays an important role in the electrochemical intercalation process. The proposed electronic model of intercalation is universal and has outstanding significance with regard to tailoring the properties of electrode materials to the most efficient application in Li-ion and Na-ion batteries. The paper reveals correlation between electronic structure, transport, and electrochemical properties of layered Li_xCoO_2 , $Li_xNi_{1-y-z}Co_yMn_zO_2$ and Na_xCoO_2 cathode material and explains of apparently different character of the discharge/charge curve in Li_xCoO_2 (monotonous curve) and Na_xCoO_2 systems (step-like curve). Comprehensive experimental studies of physicochemical properties of $Li_xNi_{1-y-z}Co_yMn_zO_2$ cathode material (XRD, electrical conductivity, and thermoelectric power) are supported by electronic structure calculations performed using the Korringa-Kohn-Rostoker method with the coherent potential approximation (KKR-CPA) to account for chemical disorder. It is found that even small oxygen defects ($\sim 1\%$) may significantly modify DOS characteristics via formation of extra broad peaks inside the former gap leading to its substantial reduction.

Keywords: lithium and sodium intercalation, electronic structure, Li_xCoO_2 , $Li_xNi_{1-y-z}Co_yMn_zO_2$, Na_xCoO_2

1. Introduction

Lithium or sodium intercalation into layered MO_2 transition metal oxides involves both ions and electrons, and can be expressed by the equations:



This reaction involves energy at the level of several eV/atom, which is associated with deep d -type electron levels in transition metal compounds. This enables the storage of several hundred Wh/kg and makes it possible to build power sources with high volumetric and gravimetric energy density.

The many years of the author's studies of various transition metal compounds: Li_xTiS_2 and Na_xTiS_2 [1], Li_xCoO_2 [2], Na_xCoO_2 [3–6], Li_xVO_2 [7, 8], $\text{Li}_x\text{W}_y\text{V}_{1-y}\text{O}_2$ [9], LiNiO_2 [10], Li_xWO_3 [11], $\text{Li}_x\text{YBa}_2\text{Cu}_3\text{O}_{7-\delta}$ [12, 13], $\text{Li}_x\text{Mn}_2\text{O}_4$ [14, 15], $\text{Li}_x(\text{Co,Ni,Mn})\text{O}_2$ [16], $\text{LiNi}_{0.5-y}\text{Cu}_y\text{Mn}_{1.5}\text{O}_{4-\delta}$ [17] showed that the electronic structure and transport properties of the cathode material play a significant role in the intercalation process. Experience in the field of ionic and electronic defect structure in transition metal compounds allowed the author to see the phenomenon of intercalation as an ionic-electronic process from a perspective different than the one that is commonly presented in the literature. This became a starting point for the proposition of an original concept of the intercalation process and the related phenomena [3, 14, 18, 19].

For a $\text{A/A}^+/\text{A}_x\text{MO}_2$ -type cell ($\text{A} = \text{Li}$ or Na) with a cathode material with the concentration of electronic charge carriers in A_xMO_2 determined by the concentration of intercalated alkaline ions, it can be demonstrated that the variation of the cell's electromotive force as a function of intercalation degree corresponds to variations of the Fermi level in the cathode material [4, 14]. The electromotive force (E) of a $\text{A/A}^+/\text{A}_x\text{MO}_2$ cell is the difference in the chemical potential of lithium (sodium) in the cathode and anode (metallic Li or Na) materials:

$$\mu_{\text{A(cathode)}} - \mu_{\text{A(anode)}} = -F \cdot E \quad (2)$$

Since the potential of the A/A^+ anode is constant (constant concentration of Li^+ or Na^+ ions in electrolyte), the variations of electromotive force of the cell can be ascribed to the changes in $\mu_{\text{A(cathode)}}$, i.e. $-F \cdot \Delta E = \Delta \mu_{\text{A(cathode)}}$. The chemical potential of lithium (sodium) in the cathode material can be represented as a sum of chemical potentials of lithium (sodium) ions and electrons:

$$\mu_{\text{A(cathode)}} = \mu_{\text{A}^+} + \mu_e \quad (3)$$

Since the chemical potential of lithium (sodium) ions can be expressed as:

$$\mu_{\text{A}^+} = \mu_{\text{A}^+}^0 + k_B T \cdot \ln [\text{A}^+] \quad (4)$$

thus:

$$\Delta \mu_{\text{A}^+} = k_B T \ln \frac{[\text{A}^+]_f}{[\text{A}^+]_i} \quad (5)$$

where f and i denote the final and initial states, respectively.

The chemical potential of electrons in the cathode material can be identified as the energy of the Fermi level; the changes in the latter are determined by the electronic structure (DOS—density of states) in the vicinity of E_F , and can vary in the range of 1 eV or more upon the introduction of electrons during lithium (sodium) intercalation. For a change in lithium (sodium) ion concentration that is of the order of 1 mole ($\Delta [\text{A}^+] \sim 1$), the change in the chemical potential of lithium (sodium) ions in the cathode material ($\Delta \mu_{\text{A}^+}$) is of the order of $k_B T$, i.e. only 0.025 eV at the room temperature (Eq. (5)), while the change in the chemical potential of electrons in the cathode material may be as much as two orders of magnitude higher ($\Delta \mu_{\text{A}^+} \ll \Delta \mu_e$). Therefore, the variations of the electromotive force of the $\text{A/A}^+/\text{A}_x\text{MO}_2$ cell which accompany the intercalation reaction correspond mainly to those in the chemical potential of electrons (i.e. Fermi level variations) of the cathode material. **Figure 1** shows the electronic scheme of the $\text{A/A}^+/\text{A}_x\text{MO}_2$ cell and depicts the difference in the chemical potentials of electrons

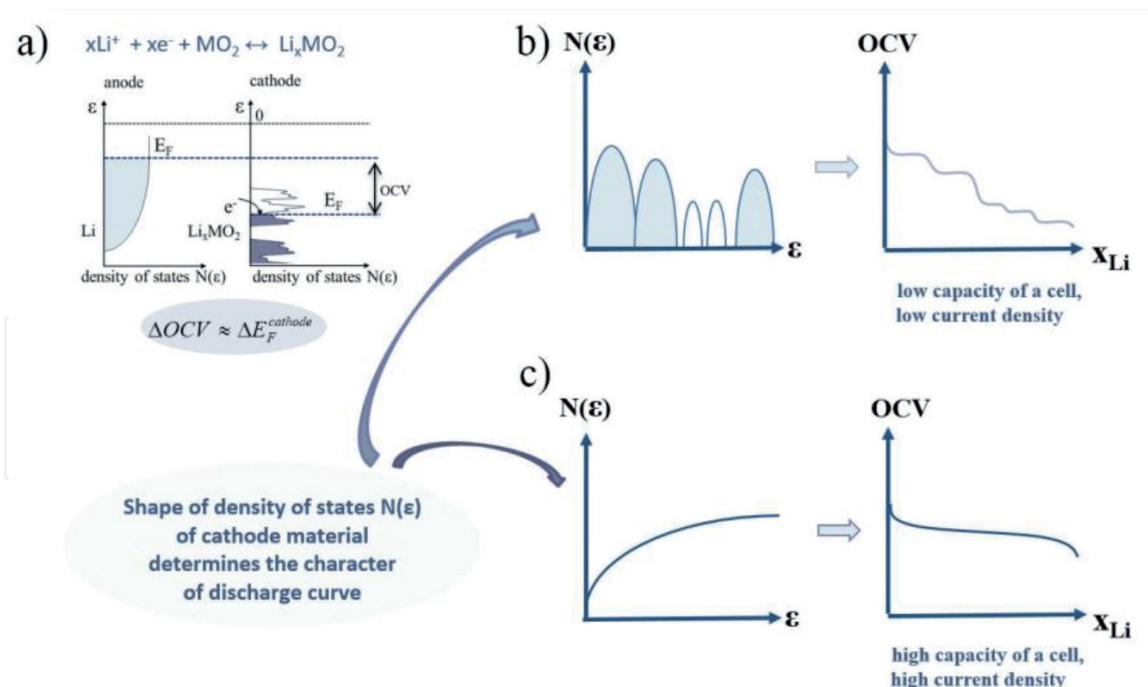


Figure 1.
 (a) Density of states of Li_xMO_2 and lithium illustrating difference in chemical potential of electrons and resulting electromotive force of $\text{Li}/\text{Li}^+/\text{Li}_x\text{MO}_2$ cell. Expected character of the discharge curve (EMF) of the $\text{Li}/\text{Li}^+/\text{Li}_x\text{MO}_2$ cell, depending on the electronic structure of the cathode material (step-like (b) and monotonic (c)).

in the cathode and anode materials and the related electromotive force of the cell. The electrons inserted into the cathode material during intercalation together with an equivalent number of lithium (sodium) ions (Eq. (1)) occupy the available electronic states at the Fermi level and raise it in a way dependent on the profile of the density of states function.

The character of the density of states function determines the shape of the discharge curve (monotonic or step-like). **Figure 1b** and **c** illustrate the correlation between the electronic structure of a cathode material and the nature of its discharge curve. A continuous density of states function in a cathode material leads to a monotonic discharge curve that is beneficial from the point of view of practical application (**Figure 1c**), while a discontinuous density of states function leads to an adverse, step-like nature of the discharge curve (**Figure 1b**). In addition, the localization of electronic states that accompany the discontinuous density of states function limits the kinetics of the lithium intercalation process, reducing the current density of a cell and making the utilization of the theoretical capacity of a cathode material impossible.

The proposed electronic model of electrochemical intercalation explains both the monotonic and step-like characters of the discharge curve, and allows the anticipation and engineering of the properties of intercalated electrode materials. The presented model also demonstrates that a method of studying the $\text{Li}^+/\text{Li}_x\text{MO}_2$ cathode potential by measuring the electromotive force of a $\text{Li}/\text{Li}^+/\text{Li}_x\text{MO}_2$ cell is an excellent tool with regard to experimental solid state physics, allowing the direct observation of changes in the position of the Fermi level in Li_xMO_2 during “lithium intercalation.” Similar conclusions are valuable for Na_xMO_2 systems.

Below we present three examples of intercalated transition metal oxides Li_xCoO_2 [5, 20], $\text{Li}_x(\text{Co}, \text{Ni}, \text{Mn})\text{O}_2$ [21] and Na_xCoO_2 [3–5], in which through the intercalation of alkali metal the controlled crossing insulator-metal can be performed, and track changes in the position of the Fermi level as a function of concentration of electrons introduced in the intercalation process (along with alkali ions).

2. Li_xCoO_2

LiCoO_2 is currently used as a cathode material in commercial Li-ion batteries, due to, among other advantages, its high voltage. Cycling with upper cut off set at 4.2 V corresponds to deintercalation/intercalation of about 0.5 Li per LiCoO_2 formula unit, and gives a specific capacity of about 140 mAh g^{-1} . Deeper deintercalation causes structural instability of the Li_xCoO_2 cathode material, loss of oxygen from the material, and its reactivity with liquid electrolyte [22–25].

LiCoO_2 exhibits hexagonal-type lattice (O_3 structure) with $R\bar{3}m$ space group symmetry (**Figure 2**). This structure consists of close-packed oxygen layers stacked in ABC-like sequence. Cobalt and lithium ions are surrounded by six oxygen atoms, forming CoO_6 and LiO_6 octahedral coordination. CoO_6 octahedra share edges creating two-dimensional arrangements (CoO_2 layers), between which van der Waals-type gap exists, occupied by lithium ions. Extraction of lithium from LiCoO_2 proceeds as a sequence of the phase transitions. For lithium content $0.95 \leq x \leq 1$ one-phase solid solution domain with hexagonal structure (hex-I) is observed. Two-phase coexistence region is found to exist between Li concentrations of $x = 0.94$ and 0.75 [20, 26–30]. These two phases share the same crystal symmetry, but show difference in the lattice parameters, mainly in the c parameter. Many authors report that for lithium content below $x = 0.75$, one phase region with hex-II phase exists [26–30]. For $x = 0.5$, a transition from hexagonal to monoclinic phase occurs, which is accompanied by a large increase of the unit cell dimension along the c -axis, up to 1.7%.

Our results, presented in papers [20], diverge with the mentioned literature data, where it is stated that hex-II phase replaces hex-I phase for the compositions with $x < 0.75$. We also do not agree with a thesis that hex-I phase exhibits semi-conducting properties, while hex-II phase shows metallic-type behavior [20]. It is known that upon lithium deintercalation crystal structure of LiCoO_2 undergoes

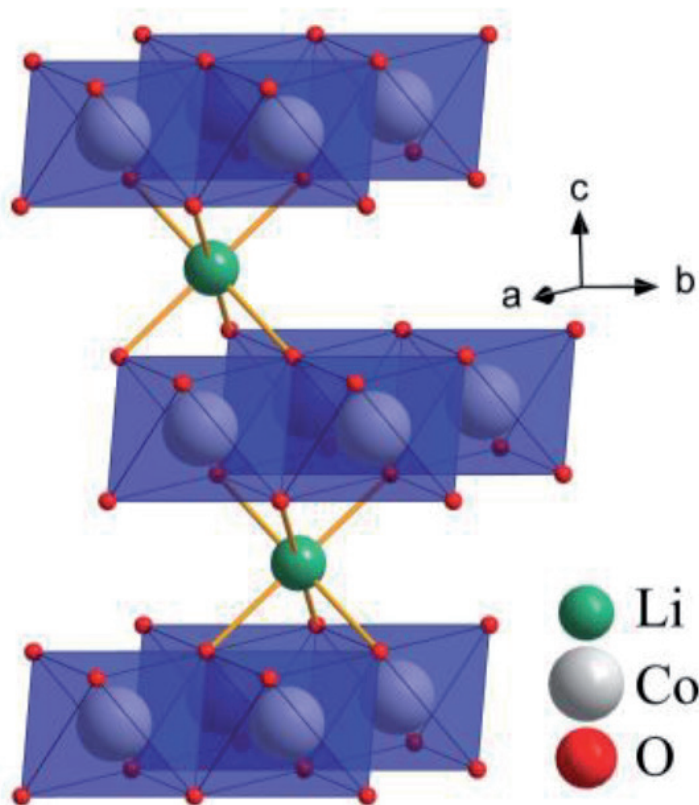


Figure 2.
Hexagonal O_3 structure of LiCoO_2 with the $R\bar{3}m$ space group.

modification. **Figure 3a** presents variations of lattice parameters of hexagonal phase of Li_xCoO_2 during deintercalation of Li. **Figure 3b** presents the mole fraction of the hex-II phase as a function of lithium content.

One can see that hex-II phase appears for $x = 0.94$ but fast disappears on further deintercalation. **Figure 3c** presents z parameter of oxygen $6c$ ($0,0,z$) position, responsible for a deformation of oxygen octahedron surrounding Co cation. While lattice parameters a and c evolve on deintercalation only slightly, z parameter changes in irregular way. Parameter z and its importance on the electronic structure of Li_xCoO_2 will be discuss later. In Li_1CoO_2 Co^{3+} cations ($3d^6$) adopt low-spin configuration ($t_{2g}^6 e_g^0$), being present in octahedral oxygen environment. Cobalt $3d$ orbitals are energetically close to oxygen $2p$ orbitals, and as a result, considerable covalent mixing, and consequently, a high degree of delocalization of the electronic states over the CoO_6 octahedra occurs [31]. Deintercalation of lithium ions from LiCoO_2 structure is accompanied by charge compensation at the Co sites, and leads to a formation of Co^{4+} ($3d^5$) states. Above 4.2 V, energy level of $\text{Co}^{3+/4+}$ redox reaction overlaps with the top of the $\text{O}2p$ band, and as a results, to the oxidation and release of the oxygen from the structure of the cathode material [31].

In this work, electronic structure calculations for Li_xCoO_2 system were performed using the Green function Korringa-Kohn-Rostoker method with the coherent potential

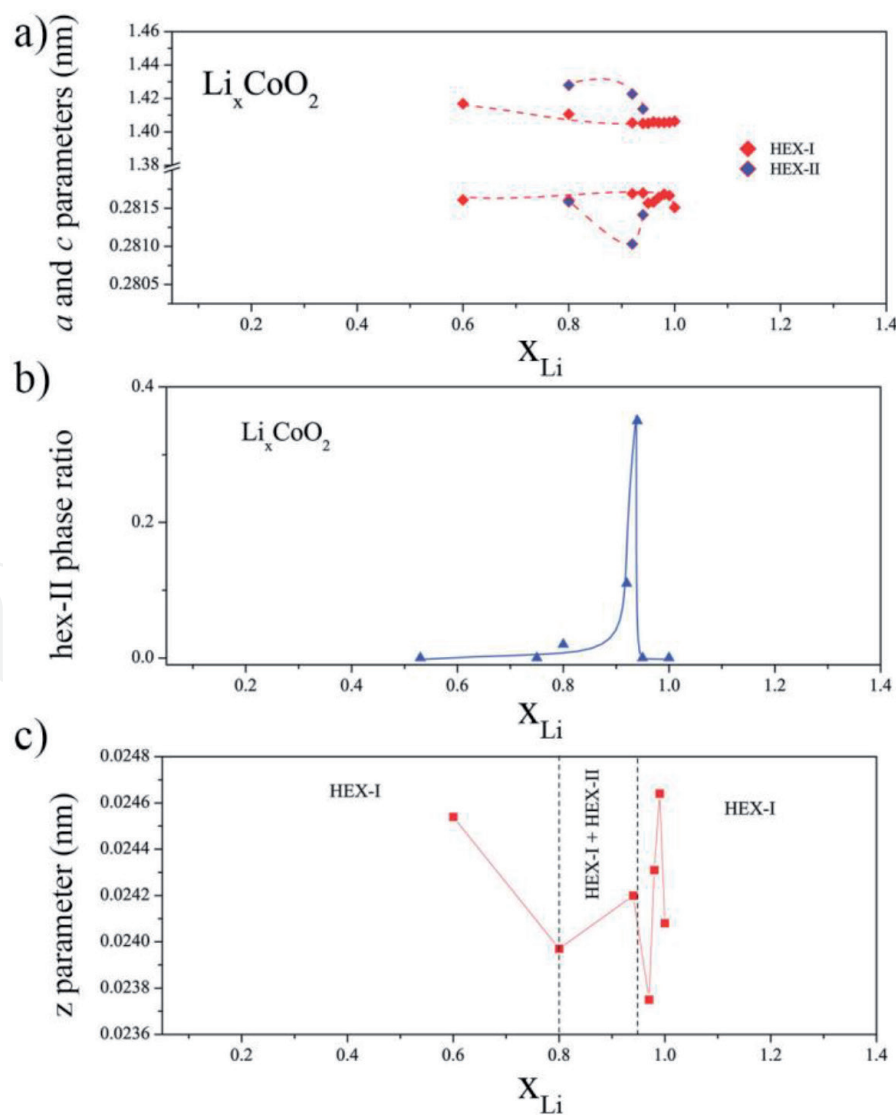


Figure 3.
 (a) Variations of lattice parameters of hexagonal Li_xCoO_2 phase during deintercalation of lithium, (b) the mole fraction of hex-II phase and (c) changes of z parameter during deintercalation of lithium.

approximation (KKR-CPA), which allows to account for chemical disorder [20, 32–34]. **Figure 4** presents such calculations for the stoichiometric LiCoO_2 and for the deintercalated Li_xCoO_2 with $x = 0.99, 0.97$ and 0.6 . Electronic structure of the starting LiCoO_2 (**Figure 4a**) consists of valence and conductivity band, separated by an energy gap of the order of 1 eV. The valence states are formed essentially from strongly hybridized d -states of Co and p -states of oxygen. Let us consider the following:

What are electronic structure predictions about the properties of Li_xCoO_2 system during deintercalation of lithium i.e. during extraction of electrons?

What about evolution of the Fermi level position and its influence on a character of the OCV curve changes occurring during charge of $\text{Li}/\text{Li}^+/\text{Li}_x\text{CoO}_2$ cell?

What about modification of transport properties of Li_xCoO_2 in this process?

For starting, stoichiometric LiCoO_2 , the Fermi level is situated in the energy gap (**Figure 4a**), so semiconducting properties should be observed. During deintercalation of lithium, the electrons are extracted from the valence band, and the Fermi level is sharply shifted to a new position in the valence band (**Figure 4b**), while further changes to its placement, occurring during the deintercalation process should be monotonous in a wide range of lithium concentration (**Figure 4b–d**). Therefore, electrical properties of Li_xCoO_2 should become more and more metallic, due to the shifting of the Fermi level in these regions, where sharp increase of the density of states appears.

In order to verify our electronic structure predictions on transport and electrochemical properties of Li_xCoO_2 system, comprehensive studies of the OCV charge curve and transport properties were conducted. **Figure 5** present charge curve (OCV) for Li_xCoO_2 . Points denotes lithium concentrations, for which the work of the

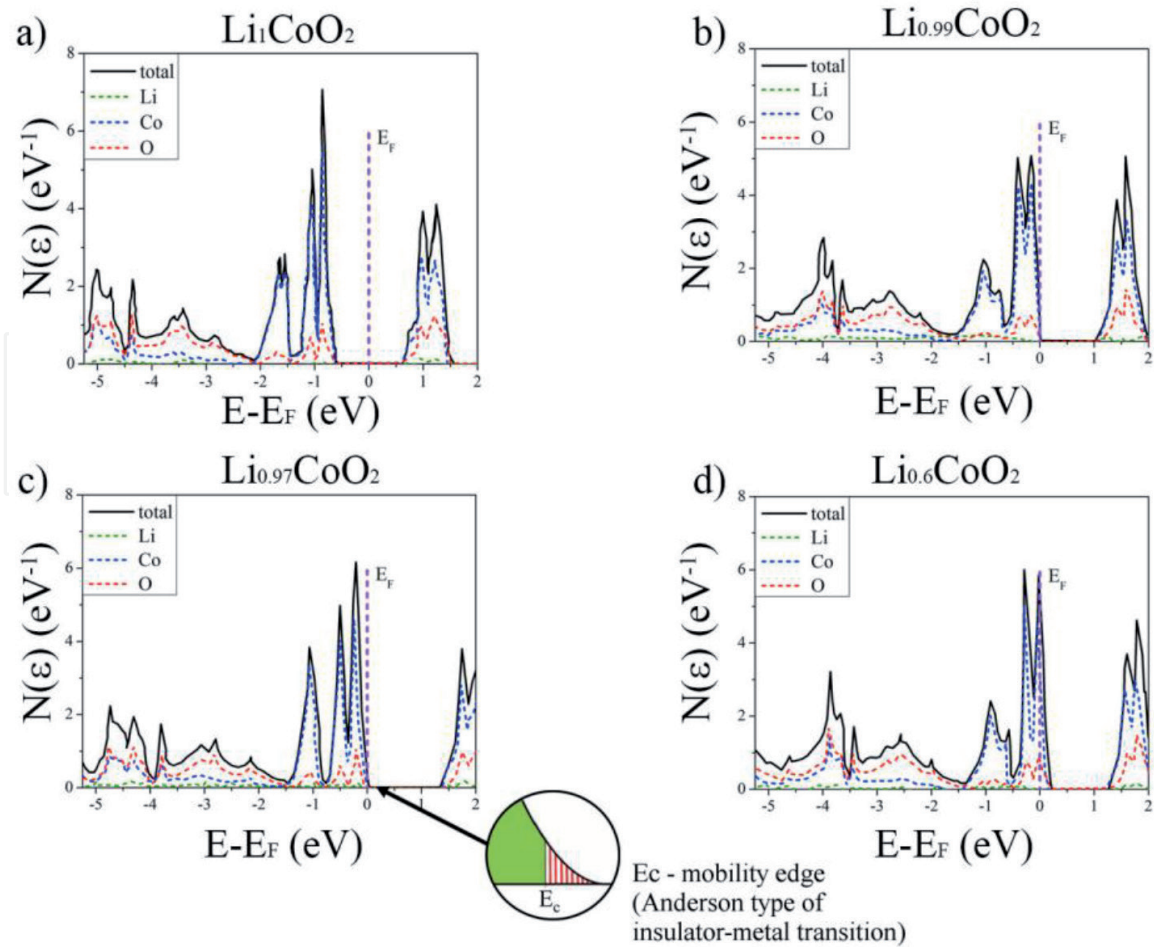


Figure 4. Electronic structure calculations (KKR-CPA) for starting LiCoO_2 and deintercalated Li_xCoO_2 for (a) $x = 1$, (b) $x = 0.99$, (c) $x = 0.97$ and (d) $x = 0.6$.

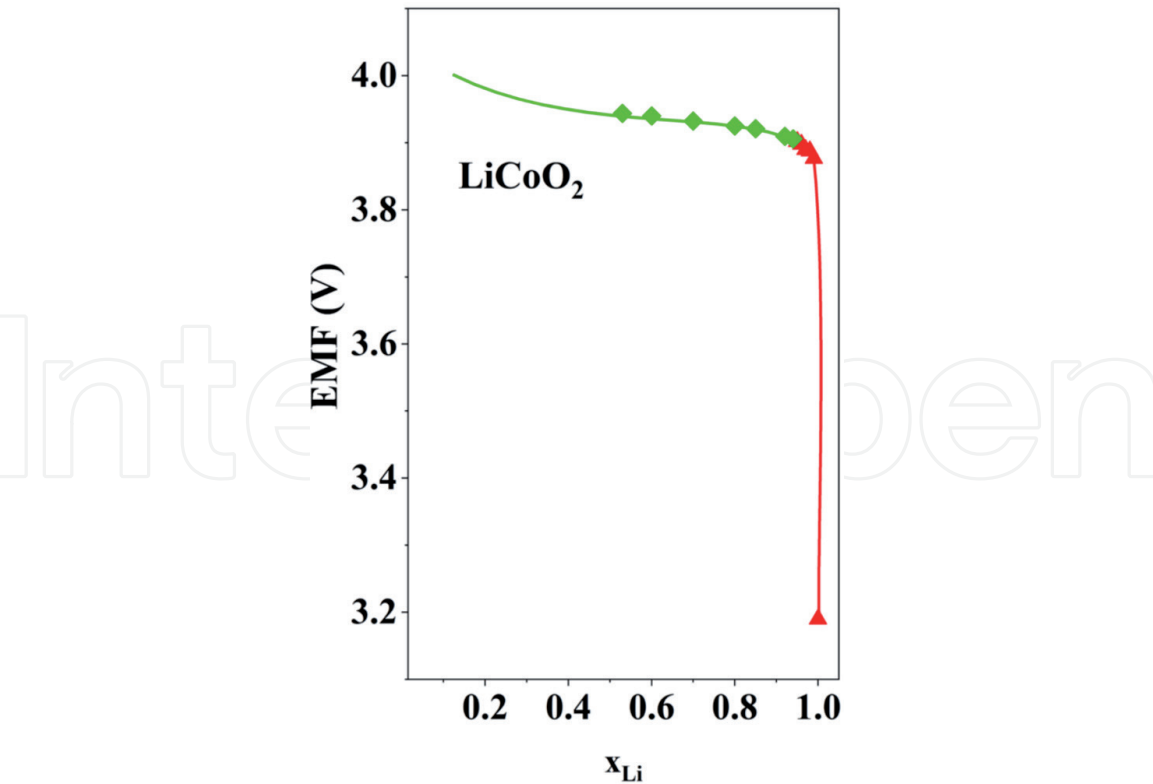


Figure 5.
Li_xCoO₂ charge curve (OCV).

cathode material was stopped in order to examine its structural properties, conduct NEXAFs measurements, as well as perform electrical conductivity and thermoelectric power studies. **Figure 6a** and **b** present temperature dependence of the electrical conductivity and thermoelectric power for Li_xCoO₂ system. Comparison and analysis of **Figures 5–7** show strong correlation between electronic structure, Fermi

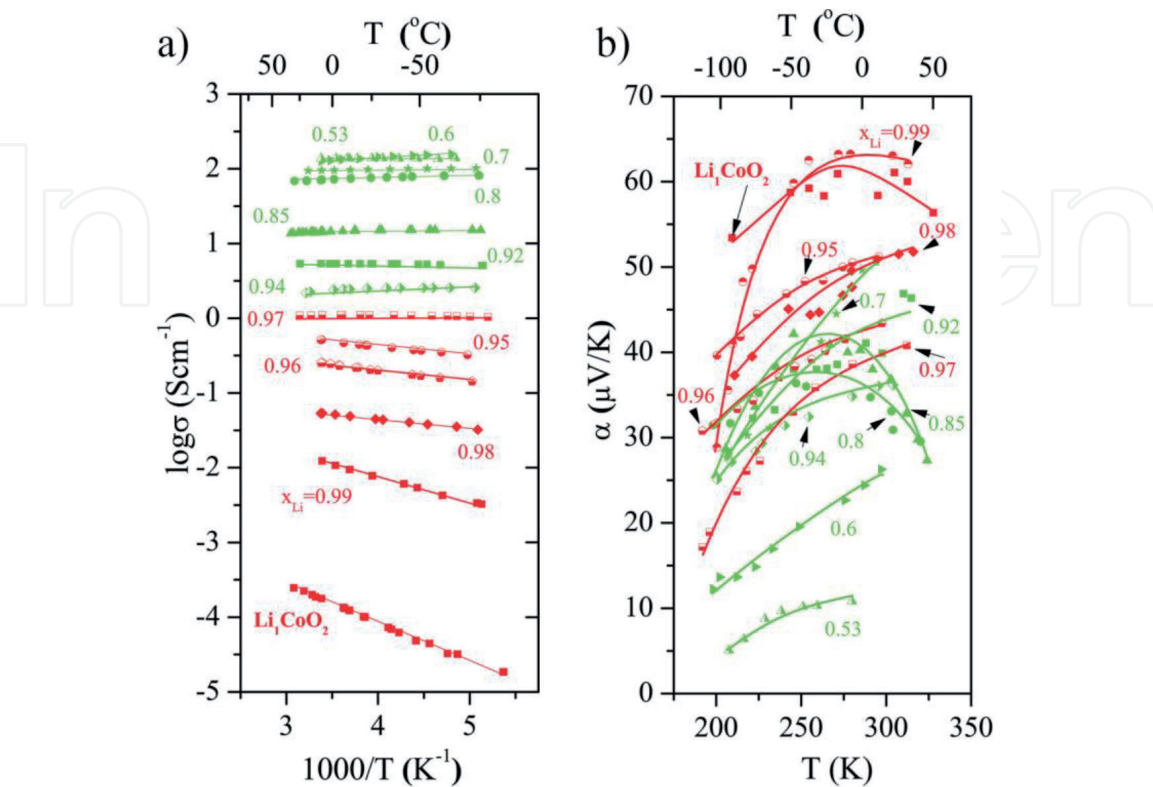


Figure 6.
Temperature dependence of (a) electrical conductivity and (b) thermoelectric power for Li_xCoO₂ system.

level variations, character of the charge/discharge curve and transport properties of Li_xCoO_2 system. For starting material, Li_1CoO_2 , Fermi level is situated in the energy gap (**Figure 4a**), so we observed semiconducting-like properties (**Figure 6a**), and a potential jump occurring at the beginning of the OCV charge curve (**Figure 5**).

Deintercalation of lithium (related to an extraction of electrons from the valence band) leads to a fast movement of the Fermi level to the valence band, followed by a monotonous changes in a wide range of lithium concentration (monotonous part of the charge curve **Figure 5**). According to our predictions, electrical properties modify toward metallic-like ones. Only for $x_{\text{Li}} = 1$ the activation energy of the electrical conductivity can be related directly to the energy gap, while for $0.94 < x_{\text{Li}} < 1$, the activation energy of the electrical conductivity is related to the activation energy of mobility of electron holes in the region of the tail of the valence band. Therefore, we postulate Anderson-type insulator-metal transition, related to a chemical disorder present in this system. The states above mobility edge E_c are localized, while these below E_c are delocalized (see insert in **Figure 4c**). For $x = 0.94$ Fermi level crosses the mobility edge E_c .

Analysis of the electronic structure of Li_xCoO_2 leads to the ascertainment that valence states do not evolve in a regular way with Li concentration (**Figure 4a–d**). Electronic spectrum for $x = 0.97$ seems to be more similar to that one for $x = 1$. To have a deeper insight into possible reasons of such peculiar behavior of the electronic structure of Li_xCoO_2 we analyzed crystallographic parameters namely, parameter z indicating position of the oxygen anions in the unit cell. It was found that the z parameter changes irregularly with lithium concentration (**Figure 3c**). We computed DOS for LiCoO_2 for different z using experimental values taken from the crystallographic data, as shown in **Figure 7** [20]. One can see that z parameter affect strongly valence DOS shape of LiCoO_2 oxide.

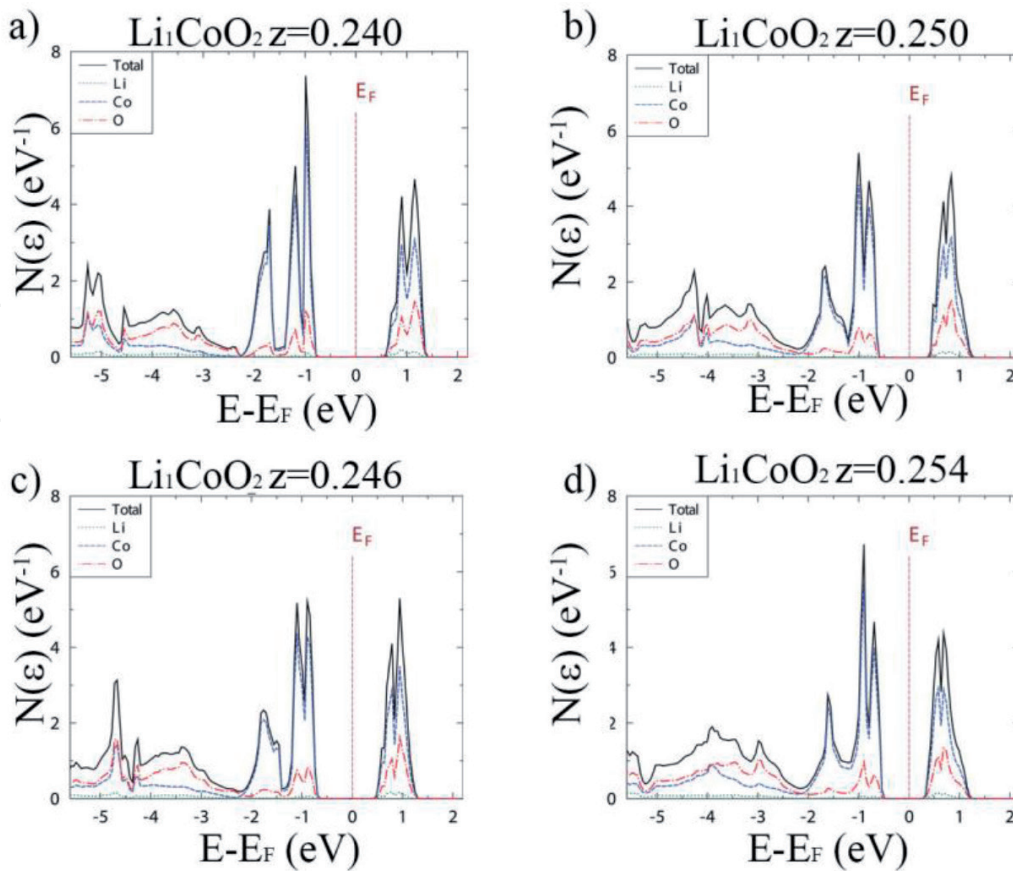


Figure 7.

(a–d) Electronic structure calculations (KKR-CPA) for LiCoO_2 for different z parameters (a) $z = 0.240$, (b) $z = 0.246$, (c) $z = 0.250$, and (d) $z = 0.254$.

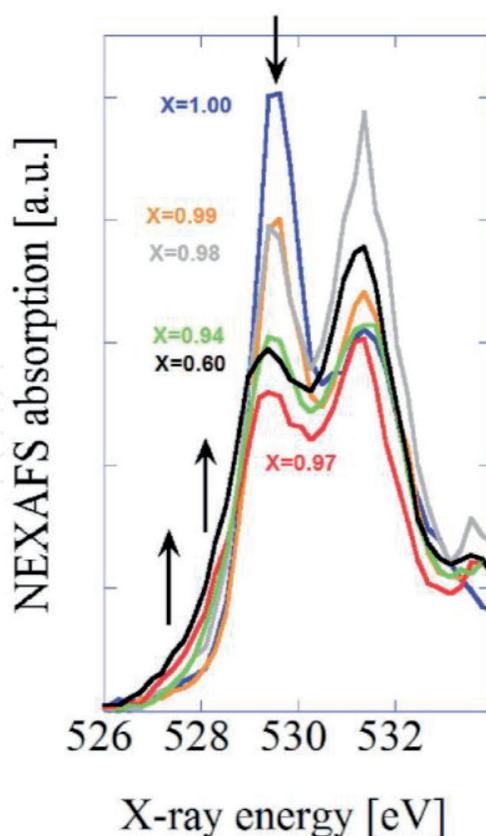


Figure 8.
 NEXAFS oxygen 1s spectra for Li_xCoO_2 samples with lithium concentration $x = 1.00, 0.99, 0.98, 0.97, 0.94$ and 0.60 .

Figure 8 shows NEXAFS oxygen 1s spectra of the Li_xCoO_2 samples with lithium concentration $x = 1.00, 0.99, 0.98, 0.97, 0.94$ and 0.60 [20]. The NEXAFS measurements of Li_xCoO_2 show a radical evolution of the top valence band features with the lithium deintercalation degree. These results corroborate well with crystallographic data, as well as with the particular effect of the oxygen octahedron distortion on the computed DOS shape (note that the respective peaks are presented in a different order on energy scale in **Figures 7** and **8**). We suppose that the z parameter (determining position of O sites), which is responsible for the deformation of oxygen octahedron surrounding Co atoms, is also responsible for modification of valence DOS, and is a reason of major discrepancies in the observed crystallographic parameters and phase diagram of Li_xCoO_2 system, presented by different authors.

3. $\text{LiNi}_{1-y-z}\text{Co}_y\text{Mn}_z\text{O}_2$

To correlate electrochemical properties of $\text{Li}_x\text{Ni}_{0.65}\text{Co}_{0.25}\text{Mn}_{0.1}\text{O}_2$ and $\text{Li}_x\text{Ni}_{0.55}\text{Co}_{0.35}\text{Mn}_{0.1}\text{O}_2$ mixed cathode materials with their transport and electronic structure properties, we stopped the work of the cathode material at the characteristic points of the charge curve (EMF, **Figure 9a**) in order to examine its properties as a function of lithium content.

The evolution of a and c parameters during the lithium deintercalation of $\text{Li}_x\text{Ni}_{0.65}\text{Co}_{0.25}\text{Mn}_{0.1}\text{O}_2$ and $\text{Li}_x\text{Ni}_{0.55}\text{Co}_{0.35}\text{Mn}_{0.1}\text{O}_2$ oxides are presented in **Figure 9b**. The a parameter decreases due to oxidation of the transition metal ions (Ni and Co) and c parameter increases due to the increase in electrostatic repulsion between $((\text{Ni}, \text{Co}, \text{Mn})\text{O}_2)_n$ sheets. The monotonic changes of the lattice parameters indicate that the crystal structure is maintained during electrochemical deintercalation of

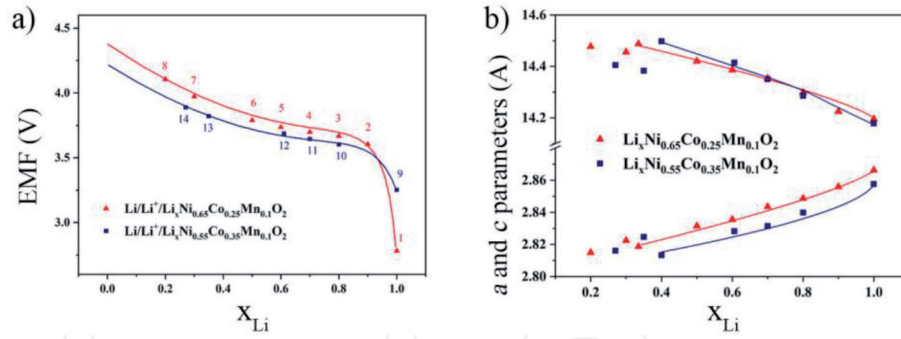


Figure 9.

(a) EMF curves for $Li/Li^+/Li_xNi_{0.65}Co_{0.25}Mn_{0.1}O_2$ and $Li/Li^+/Li_xNi_{0.55}Co_{0.35}Mn_{0.1}O_2$ cells. Points 1–14 denote lithium concentration, for which the work of the cathode material was stopped in order to study its physicochemical properties. (b) Unit cell parameters vs. Li content in $Li_xNi_{0.65}Co_{0.25}Mn_{0.1}O_2$ and $Li_xNi_{0.55}Co_{0.35}Mn_{0.1}O_2$ cathode materials.

lithium. However for lithium content lower than 0.4 mol mol^{-1} , the c parameter starts to decrease and the a parameter starts to increase that is caused due to the structural instability of the deintercalated $Li_xNi_{0.9-y}Co_yMn_{0.1}O_2$ materials in this range (oxygen ions oxidize, leave two electrons and molecular oxygen evolves from the crystal structure). Higher structural stability is observed for oxides with higher nickel content.

The temperature dependences of electrical conductivity for electrochemically deintercalated $Li_xNi_{0.65}Co_{0.25}Mn_{0.1}O_2$ and $Li_xNi_{0.55}Co_{0.35}Mn_{0.1}O_2$ oxides are presented in **Figure 10a** and **b**. The collected data show that electrical conductivity decreases with decreasing lithium concentration, and it retains its thermally activated character with activation energy of the order of $0.15\text{--}0.25 \text{ eV}$ in the entire lithium deintercalation range. However for lithium content near $x_{Li} = 0.3$, the conductivity starts to increase (**Figure 10a** and **b**). **Figure 11** presents the evolution of DOS for $Li_xNi_{0.65}Co_{0.25}Mn_{0.1}O_{2-y}$ from KKR-CPA calculations for selected Li content in the presence of oxygen vacancy as low as $y = 0.01$ [21]. From precise oxygen nonstoichiometry measurements performed for $Li_xNi_{0.65}Co_{0.25}Mn_{0.1}O_{2-y}$ oxide synthesized in air at the temperature of 850°C and quenched to room temperature, the oxygen nonstoichiometric value (y) could be estimated to be 0.06 .

Our thermogravimetric studies show a much lower value 0.014 . It is found that such defects strongly affect the electronic states particularly in the vicinity of the conductivity band edge, forming three additional DOS peaks inside the gap. Due to high degree of chemical disorder on transition metal sites, the observed ‘defect’ states are quite broad on comparing with the corresponding results in Li_xCoO_2 [20]. Interestingly, the KKR-CPA calculations deliver two important results: (i) the ‘defect’

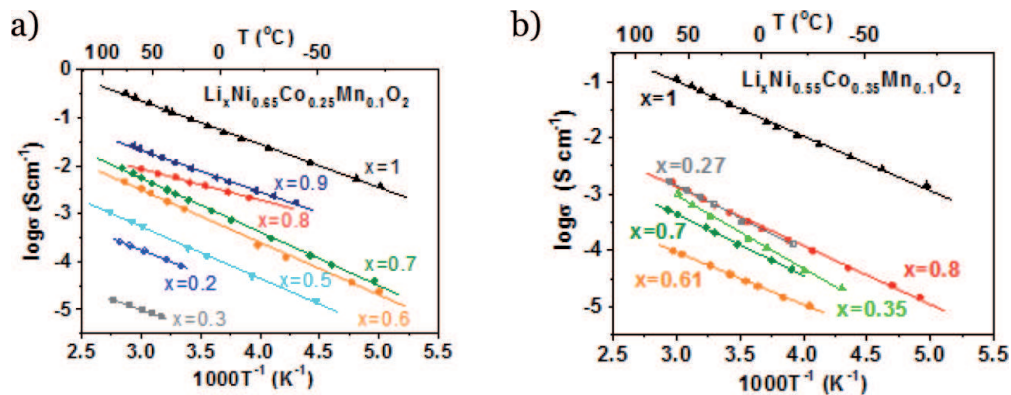


Figure 10.

Temperature dependence of the electrical conductivity of partially deintercalated (a) $Li_xNi_{0.65}Co_{0.25}Mn_{0.1}O_2$, (b) $Li_xNi_{0.55}Co_{0.35}Mn_{0.1}O_2$ oxides.

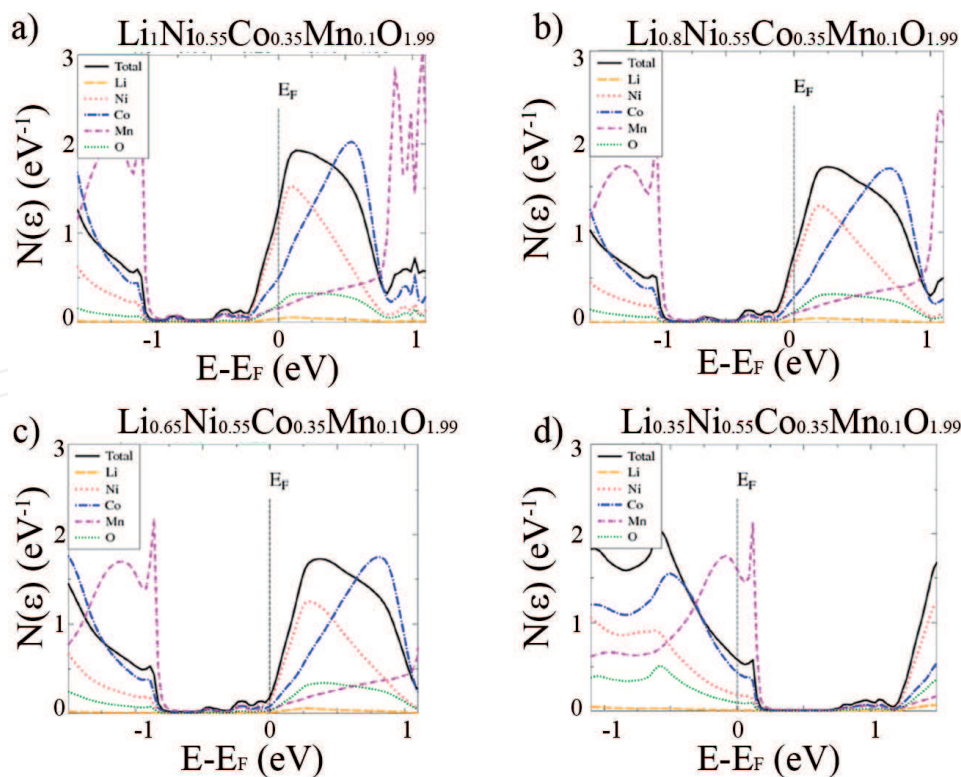


Figure 11.
(a–d) DOS in $\text{Li}_x\text{Ni}_{0.55}\text{Co}_{0.35}\text{Mn}_{0.1}\text{O}_{1.99}$ for $x = 1.0, 0.8, 0.65$ and 0.35 when accounting for oxygen vacancy concentration $y = 0.01$, as calculated by the KKR-CPA method. Total and site-decomposed DOS (per atom) are plotted (see legend). The Fermi energy (E_F) is shifted to zero. Extra peaks inside the energy are clearly observed.

states mostly contain d-states of Ni, Co and Mn, not p-states of O and, (ii) the DOS details evolve remarkably with varying Li content. Hence, it is difficult to estimate whether, in such a disordered system, the Fermi level could fall into the real gap at any Li concentration, but surely the oxygen vacancies substantially reduce the energy gap seen on DOS of LiCoO_2 [5, 20] and $\text{Li}_x\text{Ni}_{0.9-y}\text{Co}_y\text{Mn}_{0.1}\text{O}_2$ (**Figure 11**). Thus, the activation character of measured electrical conductivity could be rather related to the pseudo-gap behavior observed on DOS.

When plotting DOS at the Fermi level in the two aforementioned series of oxides (**Figure 12a**) with varied Li concentrations, we observe the finite values of DOS for all considered compositions with a deep minimum obtained for about 0.5–0.6 Li content. It is worth considering that DOS characteristics should have an important influence on electron transport properties, which are mainly governed by electronic states lying in close vicinity to the Fermi level. Indeed, the measured temperature-dependent electrical conductivity in $\text{Li}_x\text{Ni}_{0.55}\text{Co}_{0.35}\text{Mn}_{0.1}\text{O}_2$ and $\text{Li}_x\text{Ni}_{0.65}\text{Co}_{0.25}\text{Mn}_{0.1}\text{O}_2$

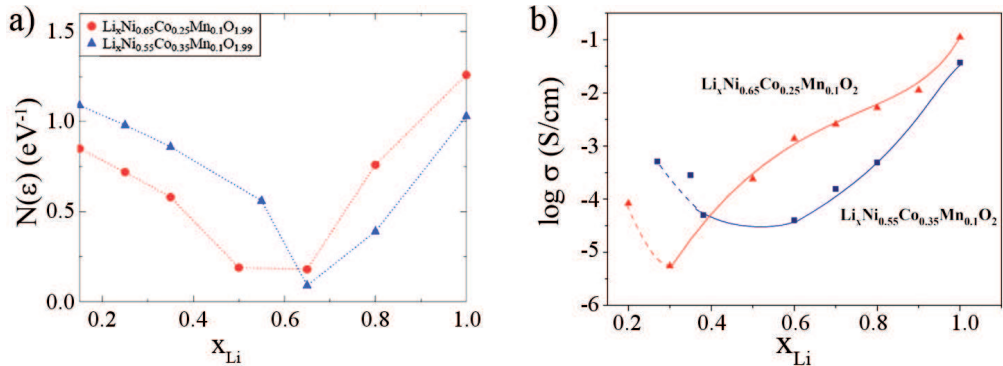


Figure 12.
(a) Variation of DOS at E_F in $\text{Li}_x\text{Ni}_{0.65}\text{Co}_{0.25}\text{Mn}_{0.1}\text{O}_{1.99}$ and $\text{Li}_x\text{Ni}_{0.55}\text{Co}_{0.35}\text{Mn}_{0.1}\text{O}_{1.99}$ and (b) conductivity with varying Li content, when accounting for oxygen vacancy concentration $y = 0.01$.

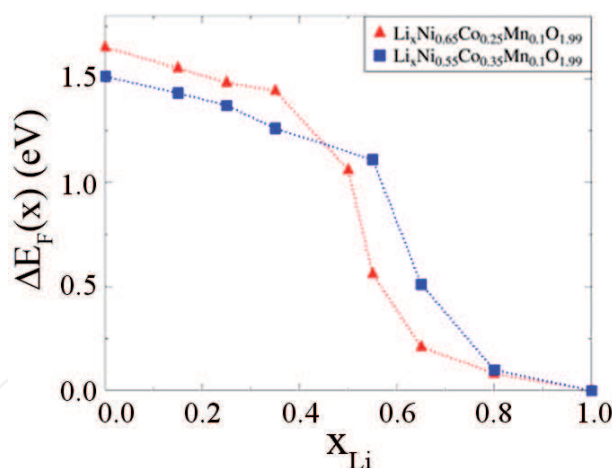


Figure 13.

Relative variation of Fermi energy (with respect to $x = 1$) with Li content of $Li_xNi_{0.55}Co_{0.35}Mn_{0.1}O_{2-y}$ and $Li_xNi_{0.65}Co_{0.25}Mn_{0.1}O_{2-y}$ cathode materials.

exhibit rather irregular behaviors with varying Li content (**Figure 10**), which could be tentatively interpreted by the variable character of the corresponding DOS curves. Such electronic structural behaviors cause both types of charge carriers, electrons and holes, to conduct electrical current in these materials. Furthermore, the character of electrical conductivity curves is mainly guided by competition between semiconducting like vs. metallic-like character.

Figure 12b shows variation of electrical conductivity of $Li_xNi_{0.65}Co_{0.25}Mn_{0.1}O_{2-y}$ and $Li_xNi_{0.55}Co_{0.35}Mn_{0.1}O_{2-y}$ in function of lithium content at room temperature. Strong correlation between the electronic structures of layered $Li_xNi_{0.9-y}Co_yMn_{0.1}O_{2-y}$ cathode materials and its electron transport properties was evidenced with characteristic minimum for $0.5 < x_{Li} < 0.6$ for both DOS and electrical conductivity (**Figure 12**).

The observed variations of the electromotive force of the $Li/Li^+/Li_xNi_{0.9-y}Co_yMn_{0.1}O_{2-y}$ cells are in good agreement with the calculated variations of chemical potential of electrons (i.e. the Fermi level variations) of the $Li_xNi_{0.9-y}Co_yMn_{0.1}O_{2-y}$ cathode material. **Figure 13** presents calculations of relative variation of Fermi energy (with respect to $x = 1$) with Li content. It is interesting to note that difference of the Fermi energy for the whole range of Li content is at the order of 1.5 eV, which corresponds well to the variation of EMF of the $Li/Li^+/Li_xNi_{0.9-y}Co_yMn_{0.1}O_{2-y}$ cell (**Figure 9a**).

4. Na_xCoO_{2-y}

Sodium analogue to $LiCoO_2$ has been extensively investigated as a potential candidate Na-intercalation-type cathode material [6, 35]. Na_xCoO_2 exhibits different electrochemical behavior, comparing to $LiCoO_2$ and shows subtle, but important differences in the crystal structure. Na_xCoO_2 presents step-like character of the discharge curve, which in according to electronic model of intercalation is surprising for the metallic system.

P2-type structure of Na_xCoO_2 ($x \approx 0.7$) consists of Na layers, which are stacked between layers of edge sharing CoO_6 octahedra (**Figure 14**). In this structure sodium occupies two different types of trigonal prismatic site: Na(1), which shares only faces with two CoO_6 octahedra of adjacent slabs, whereas Na(2) shares edges with the six surrounding CoO_6 octahedra. In addition, it can be expected that Na(1) site is less favorable energetically, due to a stronger electrostatic repulsion from the Co ions, but simultaneous occupation of Na(1) and Na(2) sites results in a

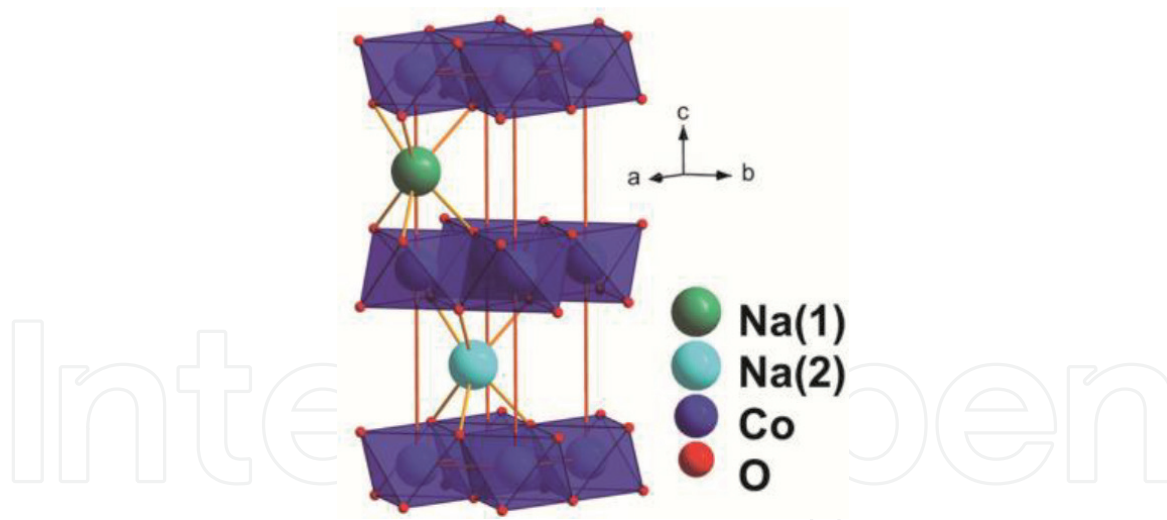


Figure 14.
 Two different crystallographic sites of sodium in the $\text{Na}_x\text{CoO}_{2-y}$ structure.

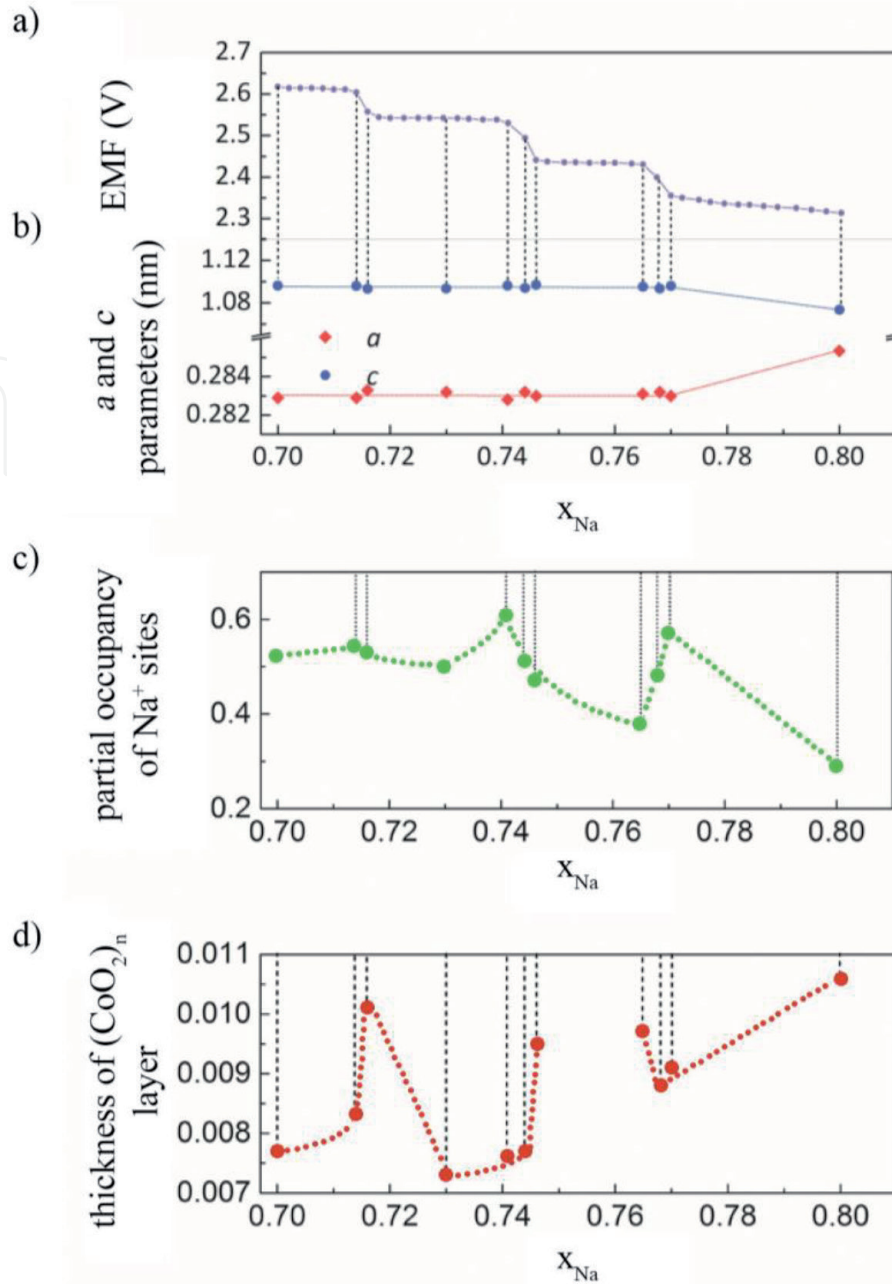
larger average Na-Na distance, comparing to a situation when only Na(2) sites are occupied. Changes of Na(1) to Na(2) ratio as a function of Na content give rise to a multitude of different types of Na ordering motifs, which can be grouped in three main pattern types: row-like, zigzag-like and droplet-like [36, 37].

Na_xCoO_2 is a potential material for thermoelectric applications due to high absolute values of thermoelectric power and metallic-type character of the electrical conductivity [38]. Sodium cobaltate exhibits superconductivity only in a narrow range of sodium content ($1/4 < x < 1/3$) below 4.5 K in the hydrated compound [39]. Occurrence of superconductivity is likely related to the lattice dimensionality and modification of the density of states near Fermi level, however, it seems that water molecules are not only passive lattice spacers [40].

The structural properties of the CoO_2 layers in Na_xCoO_2 and Li_xCoO_2 significantly affect electronic structure of these compounds. Generally, it can be stated that two-dimensional metallic CoO_2 layers, in which cobalt exists as Co^{3+} and Co^{4+} ions, which are separated by intercalating Li^+ or Na^+ ions layers, are a source of specific electronic, magnetic and electrochemical properties. Near $x = 0.5$, $\text{Co}-\text{O}$ bond length and in-plane $\text{Co}-\text{Co}$ distance are quite similar in Na_xCoO_2 and Li_xCoO_2 [41]. These parameters and thickness of CoO_2 layers increase significantly with the increasing x in Na_xCoO_2 , while in Li_xCoO_2 they change only slightly.

It may be a consequence of a relatively large size of sodium cations (0.104 nm), which gives rise to a dramatic expansion of thickness of CoO_2 layers in Na_xCoO_2 . According to the differences between geometry of CoO_2 layers in sodium and lithium system for $0.5 < x < 1.0$ range, it may be assumed that more intensive changes in the electronic band occupancy would occur in Na_xCoO_2 than in Li_xCoO_2 . **Figure 15** presents step-like character of the OCV discharge curve for $\text{Na}/\text{Na}^+/\text{Na}_x\text{CoO}_{2-y}$ cell. The work of the cathode material was stopped in the characteristic points of the discharge curve, i.e. on the potential pseudo-plateau and on the potential jumps, in order to examine its structural, transport and thermal properties. Precise structural investigations of the $\text{Na}_x\text{CoO}_{2-y}$ cathode material in equilibrium (fully relaxed cathode material) at characteristic points of a $\text{Na}/\text{Na}^+/\text{Na}_x\text{CoO}_{2-y}$ cell's discharge curve, i.e. on "potential pseudo-plateaus"¹ and potential jumps, pointed to a single-phase system in the sodium content range of 0.55–0.9, i.e. in the region where the step-like character of discharge curve is observed. The obtained results show no significant dependence of parameters a and c on the amount of sodium in the range where the

¹ Precise measurements of potential at the plateau indicate its decrease with sodium content.

**Figure 15.**

(a) Step-like character of an OCV discharge curve for the $Na/Na^+/Na_{0.7}CoO_{2-y}$ cell, (b) evolution of lattice parameters with sodium content, (c) partial occupancy of two Na^+ sites, (d) parameter z indicating the distortion of CoO_6 —oxygen octahedra.

potential jumps appear (**Figure 15b**); however, the occupancy of the two different Na sites and parameter z (thickness of CoO_2 layers, indicating CoO_6 -octahedra distortion) exhibit maxima in the area of potential jumps (**Figure 15c and d**, respectively).

Below we present the results of electronic structure calculations of Na_xCoO_{2-y} performed by KKR-CPA technique (the Korringa-Kohn-Rostoker method combined with coherent potential approximation) [3, 32, 33], which take into account the chemical disorder in the system arising from the presence of oxygen vacancies and the two different crystallographic sites of sodium. Our calculations [3] show that there is no effect of sodium sublattice ordering on the electronic structure of $Na_{0.75}CoO_2$. For four different crystallographic configurations of sodium, only very small changes in the shape of the valence band are observed, and no extra defect bands in the energy gap. **Figure 16b** presents the influence of the non-stoichiometry in oxygen sublattice on the electronic structure of $Na_{0.75}CoO_{2-y}$ calculated by KKR-CPA method. The combination of defects at two different O sites leads to

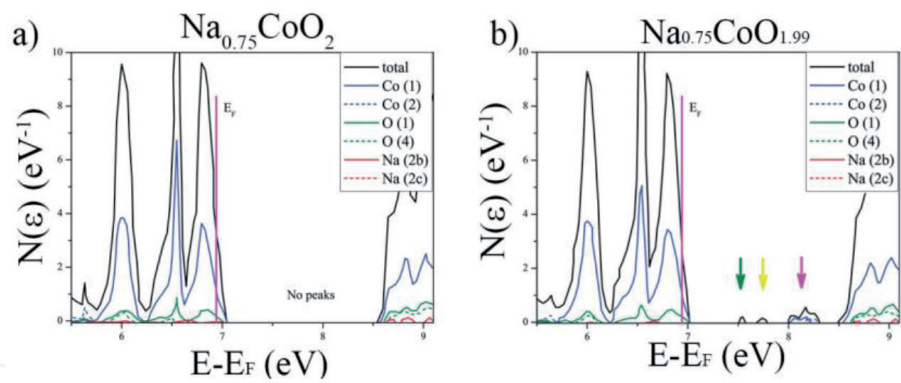


Figure 16. KKR-CPA total and site-decomposed DOS for $\text{Na}_{0.75}\text{CoO}_2$ without oxygen vacancies (a) and nonstoichiometric $\text{Na}_{0.75}\text{CoO}_{1.99}$ (b).

three extra defect bands in the energy gap, formed essentially from 3d-Co and 2p-O states. To put this into context: for strictly stoichiometric $\text{Na}_{0.75}\text{CoO}_2$, there are no extra defect bands in the energy gap (**Figure 16a**).

Figure 17a presents an electronic model of a $\text{Na}/\text{Na}^+/\text{Na}_x\text{CoO}_{2-y}$ cell, with the proposed electronic structure of $\text{Na}_x\text{CoO}_{2-y}$ (KKR-CPA calculations), which explains the step-like character of the discharge curve. In this structure, one can distinguish a valence band separated from the conductivity band by a 0.7 eV gap.

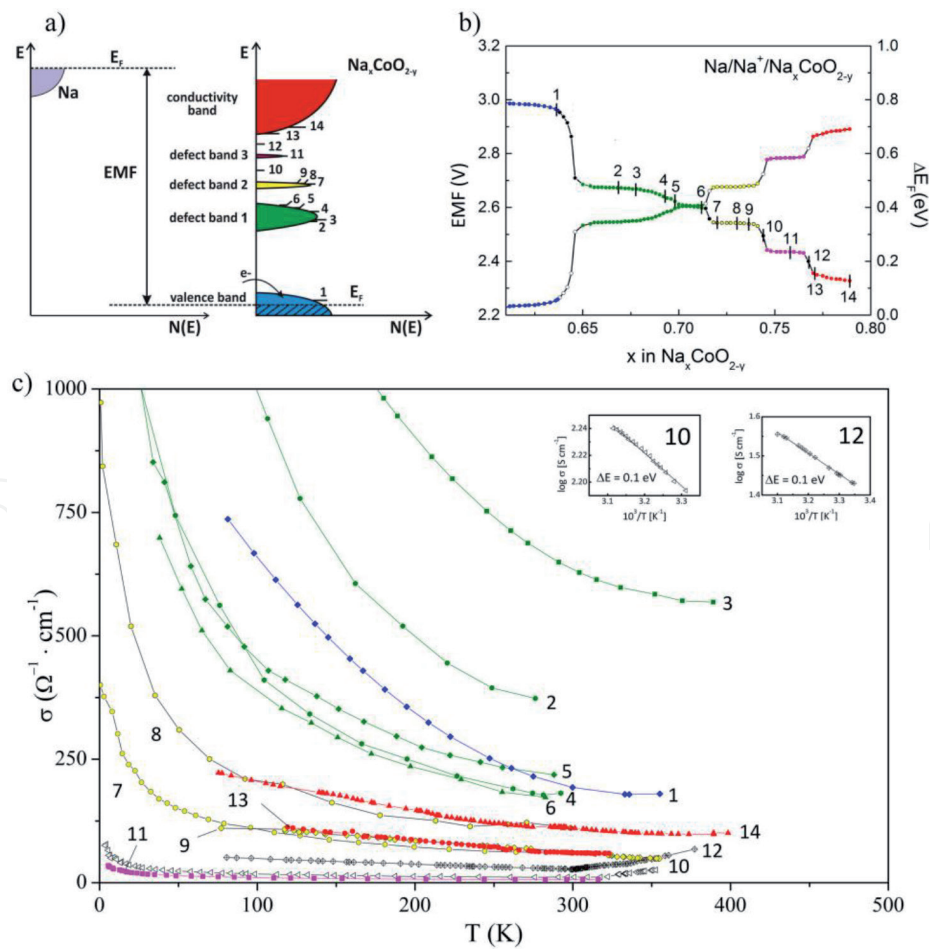


Figure 17. (a) Electronic diagram of a $\text{Na}/\text{Na}^+/\text{Na}_x\text{CoO}_{2-y}$ cell and a schematic diagram of the density of states for $\text{Na}_x\text{CoO}_{2-y}$ calculated via KKR-CPA method [3, 32, 33] and measurements of transport properties. (b) Evolution of the Fermi level of $\text{Na}_x\text{CoO}_{2-y}$ and electromotive force of a $\text{Na}/\text{Na}^+/\text{Na}_x\text{CoO}_{2-y}$ cell. (c) Temperature dependences of electrical conductivity of $\text{Na}_x\text{CoO}_{2-y}$ at characteristic points of the discharge curve (corresponding to samples no. 1–14 in **Figure 17b**).

Interestingly, three additional defect bands (denoted as “defect band 1,” “defect band 2” and “defect band 3” in **Figure 17a**) are located within the band gap. Electrons introduced during sodium intercalation quickly fill the nearly fully-occupied valence band and then fill the three subsequent defect bands (**Figure 17a**); this is accompanied by an abrupt increase in the Fermi level and, in consequence, the step-like discharge curve (**Figure 17b**). Comprehensive studies of electrical conductivity, thermoelectric power, and electronic specific heat as well as oxygen K-edge NEXAFS, carried out at characteristic points of a $\text{Na}/\text{Na}^+/\text{Na}_x\text{CoO}_{2-y}$ cell’s discharge curve, i.e. on “potential pseudo-plateaus” as well as potential jumps (**Figure 17b**), confirmed the anomalous, non-monotonic evolution of transport properties as a function of sodium content: metallic/semiconducting/metallic/semiconducting/metallic/semiconducting/metallic, which indicates anomalous, peaked density of states near the Fermi level and confirms the theoretical calculations of the electronic structure for this material. **Figure 17c** presents the measured temperature characteristics of electrical conductivity, documenting that a cathode material with a composition corresponding to a “potential pseudo-plateau” (e.g. samples no. 2–6), for which the Fermi level is located within a “defect band 1,” exhibits metallic properties (cf. **Figure 17a–c**). Similarly, samples no. 7–9, at another “potential pseudo-plateau,” also exhibit metallic behavior, although not as pronounced as the previous ones, due to the location of the Fermi level within the narrower “defect band 2” (**Figure 17a**). Sample no. 11, at the subsequent “potential pseudo-plateau,” for which the Fermi level is located within the residual “defect band 3,” exhibits even worse electrical conductivity, almost at the localization edge (**Figure 17a–c**). On the other hand, the cathode material with x_{Na} at potential jumps (samples no. 10 and 12, **Figure 17b**) corresponding to the location of the Fermi level in the energy gap of the density of states (**Figure 17a**), exhibits an activated character above 300 K, with an activation energy of 0.1 eV (**Figure 17c**, inset). This activation energy corresponds to the band gap between adequate bands in **Figure 17a** and the potential jumps of 0.1 V on the discharge curve (**Figure 17b**).

In order to support the electronic nature of step-like character of the discharge curve of a $\text{Na}/\text{Na}^+/\text{Na}_x\text{CoO}_{2-y}$ cell, electronic specific heat was measured for $\text{Na}_x\text{CoO}_{2-y}$ at characteristic points of the cell’s discharge curve, as in the case of the studies of electrical conductivity and thermoelectric power. The Sommerfeld coefficient, γ (directly proportional to density of states at the Fermi level, $\gamma = \frac{1}{3} \pi^2 k_B^2 N(E_F)$), determined at characteristic points of the cell’s discharge curve, was highly consistent with electrical conductivity and thermoelectric power results, as depicted in **Figure 18** [4]. As expected, very low values of the Sommerfeld coefficient (very low density of states), of the order of $0.6\text{--}5 \text{ mJ mol}^{-1} \text{ K}^{-2}$, were observed for samples for which the Fermi level is located in the energy gaps and in the residual “defect band 3” (denoted as H, I, J, and K in **Figure 18a** and **b**). Theoretical considerations had predicted values of $2\text{--}3 \text{ mJ mol}^{-1} \text{ K}^{-2}$. The γ values for samples denoted B, C, D, and E, for which the Fermi level is located in “defect band 1,” which exhibits a higher density of states, were of the order of $30 \text{ mJ mol}^{-1} \text{ K}^{-2}$. The sample denoted as N, located in the conductivity band, with a high density of states, has a γ value of over $30 \text{ mJ mol}^{-1} \text{ K}^{-2}$. The very low value of the Sommerfeld γ coefficient for the composition of $\text{Na}_{0.5}\text{CoO}_2$ (point A), for which a potential jump is recorded at discharge curve, corresponding to the location of the Fermi level in a band gap inside the modified valence band (**Figure 18a** and **b**), remains in very good agreement with the calculated electronic structure for this composition (**Figure 18c**), where the Fermi level is clearly located in the area of a diminishing density of states.

The above-presented new and globally unique results unambiguously document the “strictly electronic nature” of the step-like character of the discharge curve of a $\text{Na}/\text{Na}^+/\text{Na}_x\text{CoO}_{2-y}$ cell. The obtained results prove that the source of the step-like

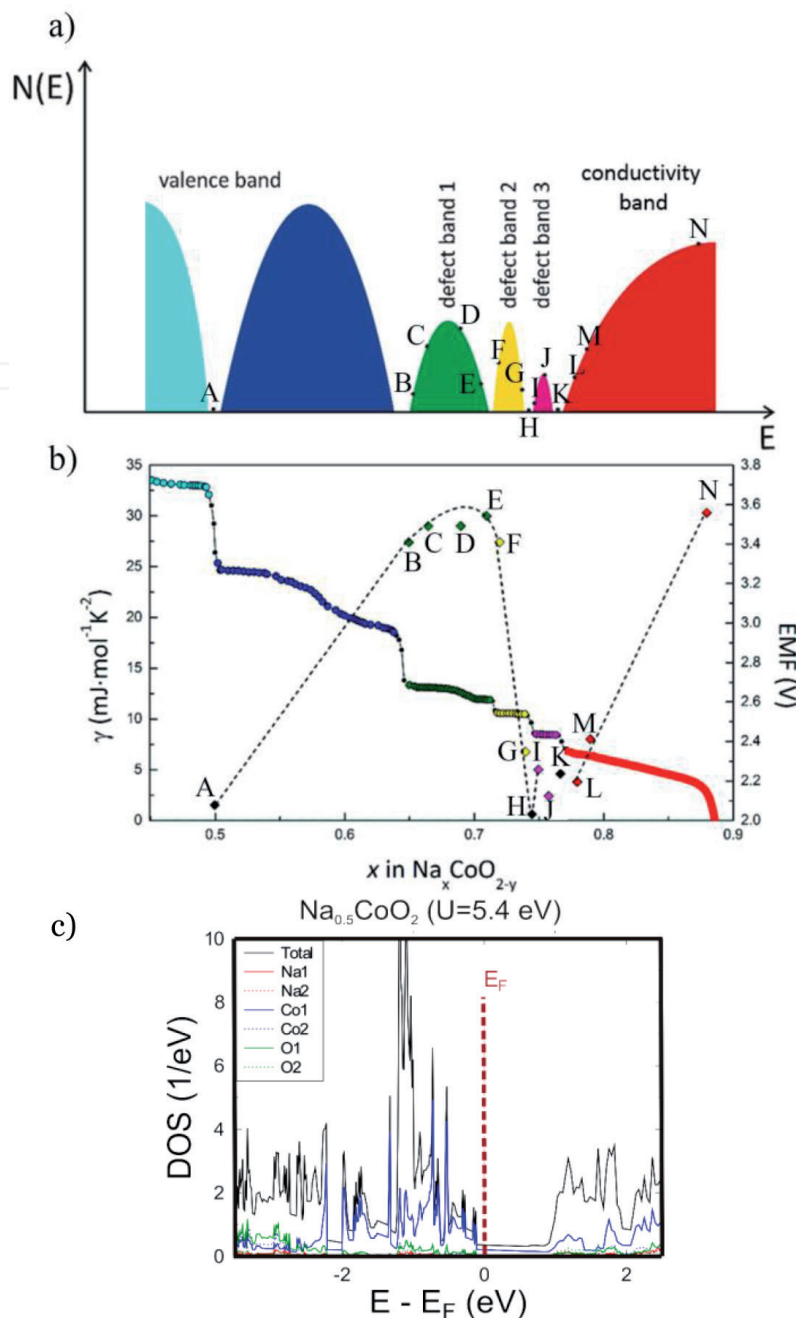
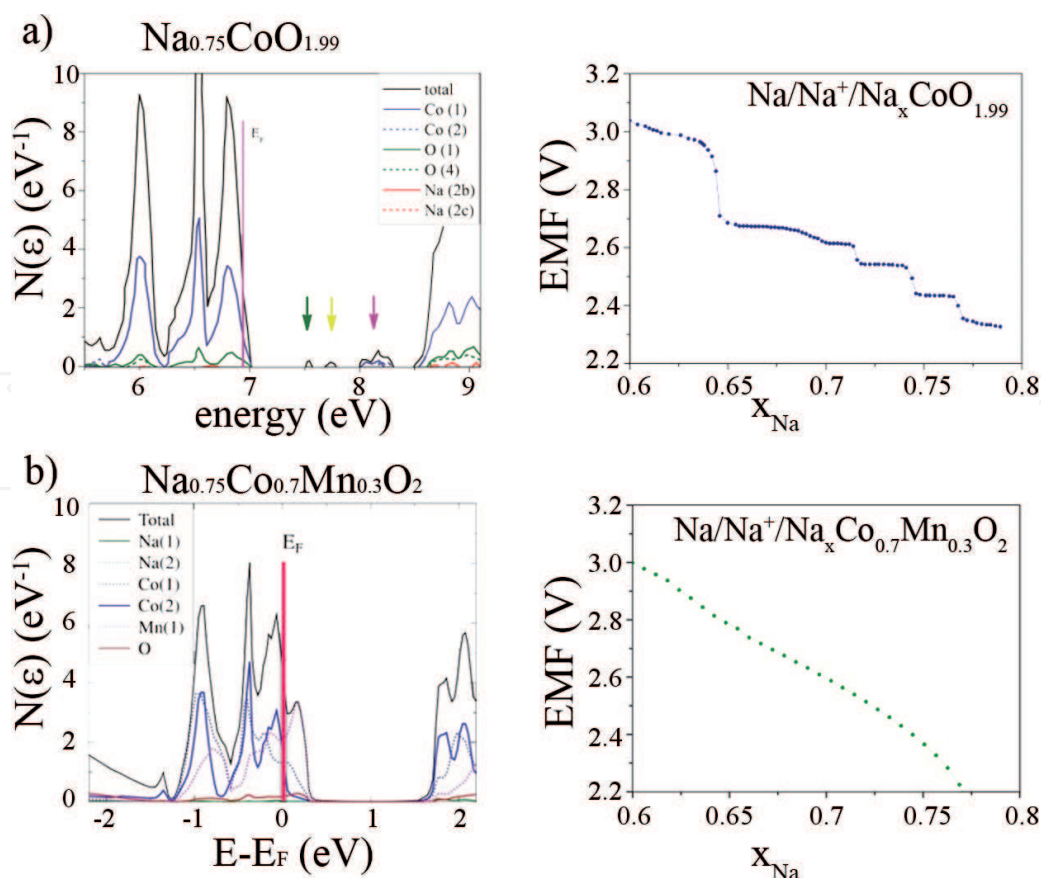


Figure 18. (a) Density of states for $\text{Na}_x\text{CoO}_{2-y}$ from KKR-CPA [3] electronic structure calculations and measurements of electrical conductivity and thermoelectric power; (b) Sommerfeld coefficient γ (points A–N) illustrating the density of states at the Fermi level in $\text{Na}_x\text{CoO}_{2-y}$ plotted against the discharge curve [4]. (c) Electronic structure of $\text{Na}_{0.5}\text{CoO}_2$ from KKR-CPA computations corresponding to point A in figures (a) and (b), U —Hubbard energy.

discharge curve of a $\text{Na}/\text{Na}^+/\text{Na}_x\text{CoO}_{2-y}$ cell is the anomalous electronic structure of the $\text{Na}_x\text{CoO}_{2-y}$ cathode material, induced by oxygen nonstoichiometry and two sodium crystallographic sites. They refute the current understanding of the principles of operation of lithium and sodium batteries, which assumes that mainly the ordering of the alkaline component and its mobility in the lithium or sodium sublattice plays a major role in the batteries parameters.

The author demonstrate that electronic structure “engineering” is a method suitable for controlling the properties of cathode materials by controlling its density of states and changing the character of the discharge curve from the unfavorable, step-like shape to the monotonic one via the modification of and control over the density of states function of a cathode material. The author has already obtained preliminary results that indicate the possibility of adjusting the properties of a

**Figure 19.**

(a) $\text{Na}_{0.75}\text{CoO}_{1.99}$ and step-like character of a discharge curve for $\text{Na}/\text{Na}^+/\text{Na}_x\text{CoO}_{1.99}$. (b) Density of states of $\text{Na}_{0.75}\text{Co}_{0.7}\text{Mn}_{0.3}\text{O}_2$ and a monotonic character of a discharge curve for $\text{Na}/\text{Na}^+/\text{Na}_x\text{Co}_{0.7}\text{Mn}_{0.3}\text{O}_2$ [42].

cathode material via the modification of the electronic structure of $\text{Na}_x\text{CoO}_{2-y}$ performed by substitution of cobalt with manganese ($\text{Na}_x\text{Co}_{1-z}\text{Mn}_z\text{O}_{2-y}$). The electronic structure calculated for this system reveals a shift of the Fermi level deeper in the valence band; as a consequence of this shift, its evolution during the electrochemical deintercalation/intercalation of sodium takes place within the valence band, resulting in a monotonic, favorable character of the discharge/charge curve for an $\text{Na}/\text{Na}^+/\text{Na}_x\text{Co}_{1-z}\text{Mn}_z\text{O}_{2-y}$ cell (**Figure 19**).

Acknowledgements

The project was funded by the National Science Centre Poland under UMO-2015/19/B/ST8/00856 and UMO-2016/23/B/ST8/00199 grants and Polish Ministry of Science and Higher Education under project AGH No. 11.11.210.911. This work was carried out using infrastructure of the Laboratory of Materials for Renewable Energy Conversion and Storage, Centre of Energy AGH.

IntechOpen

IntechOpen


Author details

Janina Molenda

Department of Hydrogen Energy, Faculty of Energy and Fuels, AGH University of Science and Technology, Krakow, Poland

*Address all correspondence to: molenda@agh.edu.pl

IntechOpen

© 2019 The Author(s). Licensee IntechOpen. Distributed under the terms of the Creative Commons Attribution - NonCommercial 4.0 License (<https://creativecommons.org/licenses/by-nc/4.0/>), which permits use, distribution and reproduction for non-commercial purposes, provided the original is properly cited. 

References

- [1] Than D, Molenda J, Stokłosa A. Correlation between electronic and electrochemical properties of $\text{Li}_x\text{Ti}_{1-y}\text{S}_2$. *Electrochimica Acta*. 1991;**36**:1555-1560
- [2] Molenda J, Stokłosa A, Bąk T. Modification in the electronic structure of cobalt bronze Li_xCoO_2 and the resulting electrochemical properties. *Solid State Ionics*. 1989;**36**:53-58
- [3] Molenda J, Baster D, Molenda M, Świerczek K, Tobola J. Anomaly in the electronic structure of the $\text{Na}_x\text{CoO}_{2-y}$ cathode as a source of its step-like discharge curve. *Physical Chemistry Chemical Physics*. 2014;**16**:14845-14857
- [4] Molenda J, Baster D, Gutowska MU, Szewczyk A, Puźniak R, Tobola J. Electronic origin of the step-like character of the discharge curve for $\text{Na}_x\text{CoO}_{2-y}$ cathode. *Functional Materials Letters*. 2014;**7**
- [5] Molenda J, Delmas C, Hagenmuller P. Electronic and electrochemical properties of $\text{Na}_x\text{CoO}_{2-y}$ cathode. *Solid State Ionics*. 1983;**9**:431-435
- [6] Molenda J, Baster D, Milewska A, Świerczek K, Bora DK, Braun A, et al. Electronic origin of difference in discharge curve between Li_xCoO_2 and Na_xCoO_2 cathodes. *Solid State Ionics*. 2015;**271**:15-27
- [7] Molenda J, Stokłosa A. Electronic structure and electrochemical properties of VO_2 . *Solid State Ionics*. 1989;**36**:43-52
- [8] Gędziorowski B, Kondracki Ł, Świerczek K, Molenda J. Structural and transport properties of $\text{Li}_{1+x}\text{V}_{1-x}\text{O}_2$ anode materials for Li-ion batteries. *Solid State Ionics*. 2014;**262**
- [9] Molenda J, Bąk T. Effect of tungsten on the electrical and electrochemical properties of the $\text{Li}_y\text{W}_x\text{VO}_2$ cathode. *Physica Status Solidi*. 1993;**135**:263-271
- [10] Molenda J, Wilk P, Marzec J. Structural, electrical and electrochemical properties of LiNiO_2 . *Solid State Ionics*. 2002;**146**:73-79
- [11] Molenda J, Kubik A. Transport properties and reactivity of tungsten trioxide. *Solid State Ionics*. 1999;**117**:57-64
- [12] Molenda J, Stokłosa A, Bak T. Transport properties of $\text{YBa}_2\text{Cu}_3\text{O}_{7-y}$ at high temperatures. *Physica C: Superconductivity and Its Applications*. 1991;**175**:555-565
- [13] Molenda J, Bak T, Stokosa A. Influence of lithium on the electronic structure of $\text{YBa}_2\text{Cu}_3\text{O}_{7-\delta}$. *Physica C: Superconductivity and Its Applications*. 1993;**207**:147-158
- [14] Molenda J, Marzec J, Świerczek K, Ojczyk W, Ziemnicki M, Molenda M, et al. The effect of 3d substitutions in the manganese sublattice on the charge transport mechanism and electrochemical properties of manganese spinel. *Solid State Ionics*. 2004;**171**:215-227
- [15] Molenda J, Marzec J, Świerczek K, Pałubiak D, Ojczyk W, Ziemnicki M, et al. The effect of 3d substitutions in the manganese sublattice on the electrical and electrochemical properties of manganese spinel. *Solid State Ionics*. 2004;**175**:297-304
- [16] Molenda J, Marzec J. Functional Cathode Materials For Li-ion Batteries - Part III: Potential Cathode Materials $\text{Li}_x\text{Ni}_{1-y-z}\text{Co}_y\text{Mn}_z\text{O}_2$ and LiMn_2O_4 . *Functional Materials Letters*. 2009;**2**:1-7

- [17] Milewska A, Kondracki L, Molenda M, Bakierska M, Molenda J. Structural, transport and electrochemical properties of $\text{LiNi}_{0.5-y}\text{Cu}_y\text{Mn}_{1.5}\text{O}_{4-\delta}$ spinel cathode materials. *Solid State Ionics*. 2014;**267**:27-31
- [18] Molenda J. Electronic Processes in Electrode Materials of A_xMX_2 -Type. *Physica Status Solidi*. 1984;**122**:591-598
- [19] Molenda J. Material problems and prospects of Li-ion batteries for vehicles applications. *Functional Materials Letters*. 2011;**4**:107-112
- [20] Milewska A, Świerczek K, Tobola J, Boudoire F, Hu Y, Bora DK, et al. The nature of the nonmetal-metal transition in Li_xCoO_2 oxide. *Solid State Ionics*. 2014;**263**:110-118
- [21] Molenda J, Milewska A, Zajac W, Rybski M, Tobola J. Correlation between electronic structure, transport and electrochemical properties of a $\text{LiNi}_{1-y-z}\text{Co}_y\text{Mn}_z\text{O}_2$ cathode material. *Physical Chemistry Chemical Physics*. 2017;**19**:25697-25706
- [22] Belov D, Yang M-H. Failure mechanism of Li-ion battery at overcharge conditions. *Journal of Solid State Electrochemistry*. 2008;**12**:885-894
- [23] Maleki H, Deng G, Anani A, Howard J. Thermal stability studies of Li-Ion cells and components. *Journal of the Electrochemical Society*. 1999;**146**:3224-3229
- [24] Dahn JR, Fuller EW, Obrovac M, Von Sacken U. Thermal stability of Li_xCoO_2 , Li_xNiO_2 and $\lambda\text{-MnO}_2$ and consequences for the safety of Li-ion cells. *Solid State Ionics*. 1994;**69**:265-270
- [25] Chen Z, Lu Z, Dahn JR. Staging phase transitions in Li_xCoO_2 . *Journal of the Electrochemical Society*. 2002;**149**:A1604-A1609
- [26] Van der Ven A, Aydinol MK, Ceder G, Kresse G, Hafner J. First-principles investigation of phase stability in Li_xCoO_2 . *Physical Review B*. 1998;**58**:2975
- [27] Marianetti CA, Kotliar G, Ceder G. A first-order Mott transition in Li_xCoO_2 . *Nature Materials*. 2004;**3**:627-631
- [28] Ménétrier M, Saadoun I, Levasseur S, Delmas C. The insulator-metal transition upon lithium deintercalation from LiCoO_2 : Electronic properties and ^7Li NMR study. *Journal of Materials Chemistry*. 1999;**9**:1135-1140
- [29] Ohzuku T, Ueda A. Solid-State redox reactions of LiCoO_2 ($R\bar{3}m$) for 4 volt secondary lithium cells. *Journal of the Electrochemical Society*. 1994;**141**:2972-2977
- [30] Mizushima K, Jones PC, Wiseman PJ, Goodenough JB. Li_xCoO_2 ($0 < x < 1$): A new cathode material for batteries of high energy density. *Materials Research Bulletin*. 1980;**15**:783-789
- [31] Chebiam RV, Kannan AM, Prado F, Manthiram A. Comparison of the chemical stability of the high energy density cathodes of lithium-ion batteries. *Electrochemistry Communications*. 2001;**3**:624-627
- [32] Kaprzyk S, Bansil A. Green's function and a generalized Lloyd formula for the density of states in disordered muffin-tin alloys. *Physical Review B*. 1990;**42**:7358-7362
- [33] Stopa T, Kaprzyk S, Tobola J. Linear aspects of the Korringa-Kohn-Rostoker formalism. *Journal of Physics. Condensed Matter*. 2004;**16**:4921-4933
- [34] Bansil A, Kaprzyk S, Mijnders PE, Tobola J. Electronic structure and magnetism of $\text{Fe}_{[3-x]}\text{V}_{[x]}\text{X}$ ($\text{X} = \text{Si}, \text{Ga}, \text{and Al}$) alloys by the KKR-CPA method. *Physical Review B*. 1999;**60**:396-412
- [35] Berthelot R, Carlier D, Delmas C. Electrochemical investigation of the $\text{P2-Na}_x\text{CoO}_2$ phase diagram. *Nature Materials*. 2011;**10**:74-80

[36] Meng YS, Hinuma Y, Ceder G. An investigation of the sodium patterning in Na_xCoO_2 ($0.5 < x < 1$) by density functional theory methods. *The Journal of Chemical Physics*. 2008;**128**:104708

[37] Hinuma Y, Meng YS, Ceder G. Temperature-concentration phase diagram of $\text{P2-Na}_x\text{CoO}_2$ from first-principles calculations. *Physical Review B*. 2008;**77**:224111

[38] Lee M, Viciu L, Li L, Wang Y, Foo ML, Watauchi S, et al. Large enhancement of the thermopower in Na_xCoO_2 at high na doping. *Nature Materials*. 2006;**5**:537-540

[39] Takada K, Sakurai H, Takayama-Muromachi E, Izumi F, Dilanian RA, Sasaki T. Superconductivity in two-dimensional CoO_2 layers. *Nature*. 2003;**422**:53-55

[40] Banobre-Lopez M, Rivadulla F, Caudillo R, López-Quintela MA, Rivas J, Goodenough JB. Role of doping and dimensionality in the superconductivity of Na_xCoO_2 . *Chemistry of Materials*. 2005;**17**:1965-1968

[41] Hertz JT, Huang Q, McQueen T, Klimczuk T, Bos JWG, Viciu L, et al. Magnetism and structure of Li_xCoO_2 and comparison to Na_xCoO_2 . *Physical Review B*. 2008;**77**:75119

[42] Baster D, Zajac W, Kondracki Ł, Hartman F, Molenda J. Improvement of electrochemical performance of $\text{Na}_{0.7}\text{Co}_{1-y}\text{Mn}_y\text{O}_{2-\delta}$ cathode material for rechargeable sodium-ion batteries. *Solid State Ionics*. 2016;**5**:213